

Coherent manipulation of a $^{40}\text{Ca}^+$ spin qubit in a micro ion trap

This article has been downloaded from IOPscience. Please scroll down to see the full text article.

2009 J. Phys. B: At. Mol. Opt. Phys. 42 154013

(<http://iopscience.iop.org/0953-4075/42/15/154013>)

[The Table of Contents](#) and [more related content](#) is available

Download details:

IP Address: 130.225.29.254

The article was downloaded on 21/09/2009 at 11:13

Please note that [terms and conditions apply](#).

Coherent manipulation of a $^{40}\text{Ca}^+$ spin qubit in a micro ion trap

U G Poschinger¹, G Huber¹, F Ziesel¹, M Deiß¹, M Hettrich¹, S A Schulz¹,
K Singer¹, G Poulsen², M Drewsen², R J Hendricks³
and F Schmidt-Kaler¹

¹ Institut für Quanteninformationsverarbeitung, Universität Ulm, Albert-Einstein-Allee 11, 89069 Ulm, Germany

² QUANTOP—Danish National Research Foundation Center for Quantum Optics, Department of Physics and Astronomy, Aarhus University, Denmark

³ Centre for Cold Matter, Blackett Laboratory, Imperial College London, Prince Consort Road, London SW7 2AZ, UK

E-mail: ulrich.poschinger@uni-ulm.de

Received 10 February 2009, in final form 9 April 2009

Published 15 July 2009

Online at stacks.iop.org/JPhysB/42/154013

Abstract

We demonstrate the implementation of a spin qubit with a single $^{40}\text{Ca}^+$ ion in a micro ion trap. The qubit is encoded in the Zeeman ground state levels $m_J = +1/2$ and $m_J = -1/2$ of the $S_{1/2}$ state of the ion. We show sideband cooling close to the vibrational ground state and demonstrate the initialization and readout of the qubit levels with 99.5% efficiency. We employ a Raman transition close to the $S_{1/2}$ – $P_{1/2}$ resonance for coherent manipulation of the qubit. We observe single qubit rotations with 96% fidelity and gate times below $5\ \mu\text{s}$. Rabi oscillations on the blue motional sideband are used to extract the phonon number distribution. The dynamics of this distribution is analysed to deduce the trap-induced heating rate of $0.3(1)$ phonons ms^{-1} .

(Some figures in this article are in colour only in the electronic version)

1. Introduction

Our research is aimed at the realization of scalable quantum simulation and information processing [1, 2]. Quantum computing with cold ions [3–6] has currently reached an experimental limit of scalability with up to eight ions if a conventional macroscopic trap is used [7]. This purely technical limitation is believed to be lifted using a segmented linear micro Paul trap, where only small groups of ions are to be kept in the quantum processing unit, and multiple trap sites are used for the storage of large-scale entanglement [8]. Several different options for encoding a qubit with a trapped ion are possible and have been realized in various groups. One might either employ superpositions of a long-lived electronic metastable state and the ground state, or alternatively use coherent superpositions of hyperfine or Zeeman ground states. In this paper, we focus on $^{40}\text{Ca}^+$ ions in a micro trap and qubits which are encoded in Zeeman sublevels of the $S_{1/2}$ ground state. We will discuss in detail how these qubits

are initialized, coherently manipulated and how finally the quantum information is read out with high fidelity. With the ion cooled close to its vibrational ground state, we are well set for two-qubit quantum logic gate operations in a multi-segmented linear micro trap, a scalable approach to ion quantum processing.

The paper is organized as follows. First, we give a brief overview on the experimental apparatus used including the micro trap and the various laser sources. In section 3, we discuss the advantages of our choice of Zeeman ground state superpositions for the qubit encoding. Two basic steps for qubit utilization, namely state preparation and readout, are demonstrated in section 4. Finally, we explain in detail how Raman transitions for the spin qubit manipulations are characterized (section 5) and present results for sideband cooling and coherent qubit dynamics (section 5.3). We show how phonon number distributions can be extracted from the analysis of Rabi oscillations on the blue sideband of the Raman transition and investigate the dynamics of the phonon

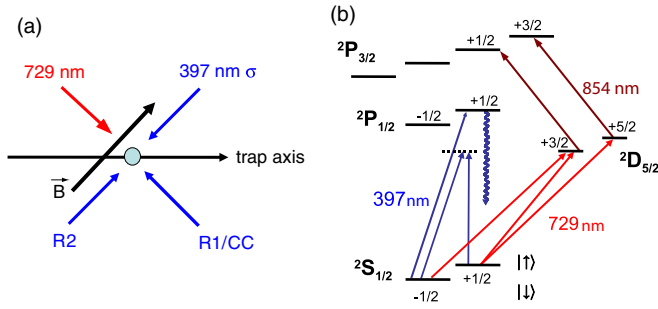


Figure 1. (a) Geometric arrangement of the lasers driving Raman (R1, R2 and CC), dipole (397 nm) and quadrupole transitions (729 nm), relative to the trap axis and magnetic field direction \vec{B} . (b) Level scheme of a $^{40}\text{Ca}^+$ ion and all relevant transitions. A magnetic field of about 6.8 G splits each fine structure level into several Zeeman components, indicated by fractional numbers.

distribution in the micro trap. The outlook sketches the future perspectives of our experiment for multi-qubit quantum logic.

2. Experimental apparatus

2.1. A segmented micro ion trap

We use a segmented linear micro ion trap. It is a sandwich structure of three alumina wafers, of which the top and bottom ones are gold coated and the middle one acts as a spacer. The trap structure is created by laser cutting with μm -scale resolution. Each trap layer consists of a RF electrode providing ponderomotive confinement in the radial plane and a set of dc electrodes for confinement in the axial direction. The RF electrodes extend along the whole length of the trap and have notches at the positions of the gaps between neighbouring dc segments in order to suppress axial bumps in the RF field. They are supplied by up to 300 V_{pp} at 24.8 MHz. The dc electrodes are supplied with voltages in a ± 10 V range by a computer-controlled battery-powered supply which is designed to provide fast and accurate voltage waveforms to the electrodes at low noise and output impedance. The ionic motion exhibits one vibrational mode along the trap axis which is to be used as the ‘bus’ mode for entangling operations. Under typical trapping conditions, when a voltage of -6 V is applied to one pair of dc segments and all other dc electrodes are grounded, an axial frequency of $\omega_{\text{ax}}/2\pi = 1.35$ MHz is measured. The radial confinement leads to two nondegenerate radial modes with typical frequencies of $\omega_{\text{rad}}^{x,y}/2\pi = \{2.0, 3.5\}$ MHz. For further details we refer to the description in [9, 10].

2.2. Laser sources and ion detection

A single ion is loaded by the photoionization of a weak neutral calcium beam by resonant two-photon photoionization [11]. Doppler cooling is achieved by means of a grating-stabilized diode laser at 397 nm, slightly red detuned with respect to the $S_{1/2}$ to $P_{1/2}$ dipole transition; see figure 1(a). As the cooling cycle is not closed, a grating-stabilized diode laser at 866 nm is

used for repumping from the metastable $D_{3/2}$ state. The light from both sources is switched by means of acousto-optical modulators (AOM). For Doppler cooling, we irradiate 100 μW and 500 μW near 397 nm and 866 nm, respectively. The waist size of both beams is about 30 μm at the ion’s location. When necessary, population in the $D_{5/2}$ state (1.2 s lifetime) can be pumped to the $P_{3/2}$ by a grating stabilized laser diode near 854 nm, followed by a fast decay to the $S_{1/2}$ ground state, which is referred to as quenching. Since the long lifetime of the $D_{5/2}$ state is important for qubit measurement, no quench light must be present during readout. To ensure sufficient extinction of the quench laser, a light of about 10 μW in a beam waist of about 50 μm is switched by a double-pass AOM. All diode lasers are locked to Pound–Drever–Hall (PDH) error signals from stable Fabry–Perot cavities which are tuned by a piezo-driven mirror.

In order to drive the $S_{1/2}$ to $D_{5/2}$ quadrupole transition, we use an amplified diode laser system. This laser source near 729 nm is PDH locked to an ultra-low expansion cavity in a UHV vessel. We estimate the laser linewidth to be better than 5 kHz as determined from Ramsey contrast measurements on the quadrupole transition, where coherence decay times of up to 200 μs were observed. The laser light near 729 nm is switched and modulated by a double-pass AOM controlled by a versatile function generator⁴ (VFG), a DDS/FPGA based RF source [12]. This allows for generation of laser pulses with almost arbitrary frequency, phase and amplitude profiles. The resulting laser beam has a power of up to 140 mW and is focussed down to roughly 10 μm , allowing Rabi frequencies up to 1.5 MHz on the $S_{1/2}, m_J = +1/2$ to $D_{5/2}, m_J = +5/2$ transition. The polarization is chosen to be at an angle of 45° to the quantizing magnetic field, whereas the propagation direction is orthogonal to it. This way, all allowed transitions between the Zeeman sublevels of the $S_{1/2}$ and $D_{5/2}$ states become accessible [4] (figure 1). The beam enters at an angle of 45° with respect to the trap axis, allowing for momentum transfer to the axial and the radial modes. We calculate the coupling to ion motion (Lamb–Dicke factors) of $\eta_{\text{ax}} = 0.06$ and $\eta_{\text{rad}}^{x,y} = \{0.034, 0.026\}$.

Raman transitions between the spin levels $m_J = +1/2$ and $-1/2$ of the $S_{1/2}$ ground state are driven by two laser beams close to the strong $S_{1/2}$ to $P_{1/2}$ dipole transition. The beams are derived from a frequency doubled amplified laser diode system delivering up to 120 mW of power at 397 nm. The laser is divided into three different beams which are termed R1, R2 and CC. The Raman transitions are then driven either by the pair R1/R2 or the pair R1/CC; see figure 1(b). All Raman beams are switched and modulated by single-pass AOMs. The AOMs for R2 and CC are supplied by the same VFG source as the AOM for the 729 nm laser. The AOM for R1 is supplied by an RF synthesizer, which also serves as a phase reference for the VFG; therefore, the necessary phase stability between R1/CC and R1/R2 is guaranteed. The limit of accuracy for the relative frequency between the VFG and synthesizer was measured to be 10 mHz, which has no adverse effect, because the timescale on which a single measurement cycle is carried out is much shorter (up to 20 ms).

⁴ VFG 150, Toptica Photonics.

The 397 nm fluorescence light emitted by the ion during Doppler cooling is detected by an electron multiplier CCD camera and a photomultiplier tube. With typical fluorescence rates of 50 counts in 3 ms from a single ion with a background of about 5 counts from scattered light, we can discriminate the state with a statistical error in the sub-per mil range [4].

All laser sources are controlled by a versatile computer control program and continuously monitored by a wavemeter with 5 MHz accuracy. A typical experimental sequence consists of four steps: (a) the ion is Doppler cooled for 3 ms, (b) then it is cooled close to the ground state of the axial vibrational mode by resolved sideband cooling (section 5.3). (c) The qubit is then initialized (section 4.1), and (d) coherent manipulations are performed on the Raman transition (section 5.1). Finally, (e) the population in the $m_J = +1/2$ qubit level is shelved (section 4.2) to the $D_{5/2}$ level, and (f) the state is read out by counting 397 nm laser induced fluorescence for 3 ms. After quenching the state by light near 854 nm, the cycle (a)–(f) is repeated, typically 100 times, giving the average transfer probability on the qubit transition.

3. Qubit realizations with Ca^+ ions and arguments for a ground state spin qubit

The level scheme of Ca^+ ions allows for at least three options to encode qubit information in a long-lived superposition of two electronic quantum states. The *optical qubit* is encoded in a superposition of the ground state $|0\rangle \equiv S_{1/2}$ and the metastable state $|1\rangle \equiv D_{5/2}$. Coherent manipulations are driven directly on this quadrupole transition by laser pulses near 729 nm; an approach has been realized with great success by the Innsbruck group [13, 14]. Disadvantages to this approach are limitations to the coherence due to phase stability of the laser source at 729 nm and ambient magnetic field fluctuations, as well as the relatively small Lamb–Dicke factor which leads to a rather weak momentum kick of the laser excitation on the ion’s vibrational motion, affecting the two-qubit gate speed. The optical qubit is read out efficiently and simply by state-dependent fluorescence, as the ground state scatters photons while the $D_{5/2}$ remains dark.

Another option is to use $^{43}\text{Ca}^+$ with nuclear spin $I = 7/2$ and to encode the qubit in *hyperfine ground state levels* $|F = 4, m_F = 0\rangle$ and $|F = 3, m_F = 0\rangle$. Coherent manipulations are achieved by employing a Raman transition, which means that an ultra-stable laser source is no longer required. It is straightforward to achieve excellent relative phase stability if the two Raman beams are derived from a single laser source. However, a large frequency gap of about 3.4 GHz must be bridged with high-bandwidth AOMs. Hyperfine clock states, insensitive to the linear Zeeman effect, can be used as computational basis states [15], which greatly increases the qubit phase coherence. The qubit readout is based on state-dependent fluorescence.

For the measurements presented here we have chosen the option to encode the *qubit in spin sublevels* $|\downarrow\rangle$ and $|\uparrow\rangle$ of the ion’s electronic ground state $S_{1/2}$ $m_J = \pm 1/2$ of $^{40}\text{Ca}^+$ with $I = 0$, Zeeman split by an applied magnetic field. Quite similar work has been performed with great success by the

Oxford group [16, 17]. However, in this work the scheme for state preparation, readout and cooling is entirely different from our approach. Furthermore, the experiments were carried out in a conventional Paul trap and do not suffer from the enhanced heating rates in a microtrap.

Coherent manipulations of the spin qubit are achieved by employing a Raman transition, and the requirement of an ultra-stable laser source can then be dropped as in the case of hyperfine qubits, but a much smaller frequency splitting of about 20 MHz allows the use of simple and efficient AOMs. The high Lamb–Dicke factor of UV–Raman transitions ensures fast two-qubit gate operations. As compared to ion species with a hyperfine structure we work with a much simpler level structure reducing the experimental complications. Qubit readout, however, is more complicated since both the $|\downarrow\rangle$ and $|\uparrow\rangle$ states can scatter photons near 397 nm. In order to discriminate between the two-qubit states, the population in $|\uparrow\rangle$ must first be completely transferred to the metastable $D_{5/2}$ state. A future possibility of avoiding qubit dephasing due to its magnetic field sensitivity for the $^{40}\text{Ca}^+$ spins will be using two physical qubits (ions), in a decoherence-free subspace of Bell states to encode one logical qubit [18, 19], in the spirit of designer atoms [20].

4. Qubit preparation and readout

According to the DiVincenzo criteria [21], the initialization of qubits to a well-defined state and the readout of the full quantum state of the qubits are essential criteria for the realization of quantum information experiments. In our experiment, both steps are realized by using a narrow optical quadrupole transition at 729 nm, and both are optimized to achieve high fidelities even under the presence of experimental imperfections and noise.

4.1. State preparation via optical pumping

The common technique for preparing an initial quantum state via optical pumping employs a circularly polarized laser beam resonant with the $S_{1/2}$ to $P_{1/2}$ dipole transition at 397 nm. In this case, both birefringence by the vacuum windows and a small offset angle between the propagation direction \vec{k}_{397} and the quantizing magnetic field results in spurious polarization components. The improper polarization components deteriorate the initialization fidelity. Furthermore, as the target state is not completely dark anymore, this leads to a continuous photon scattering of Doppler cooling light, which counteracts the ground state sideband cooling (section 5.3). Therefore, we use the high spectral selectivity of the narrow quadrupole transition for optical pumping [20]. If the ion is to be initialized in the $|\uparrow\rangle$ level, the population from $|\downarrow\rangle$ is transferred to the $D_{5/2}, m_J = +3/2$ level by a pulse at 729 nm and transferred back to the ground state by the quench laser via the $P_{3/2}$ state. This cycle is repeated until the desired initialization is reached with high fidelity.

We compare two different schemes for this pumping: either we use a pulsed scheme or we switch on both light

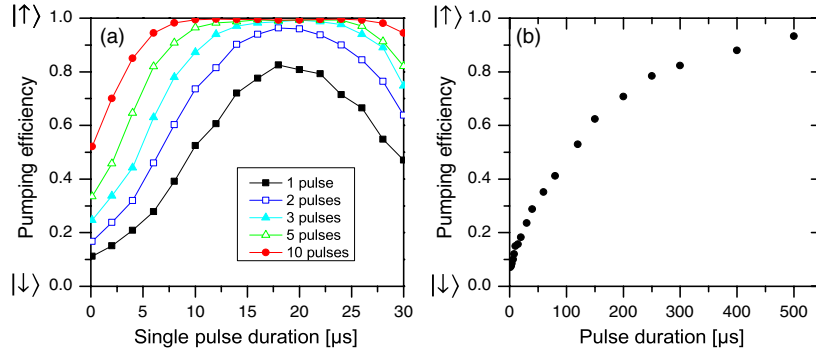


Figure 2. Single ion population is pumped by the application of circularly polarized light at 397 nm to the $|\downarrow\rangle$ state. From this state we use optical pumping by laser light at 729 nm and 854 nm to pump to the $|\uparrow\rangle$ via the $D_{5/2}, m_J = +3/2$ level. (a) Pumping efficiency of the pulsed scheme versus the 729 nm pump time of the individual pulses. The curves for various pulse numbers show how performance and robustness increase for more pulses. Note that the total duration of the pump process increases with the number of pulses. (b) The cw scheme is found less efficient.

fields continuously (figure 2). In the pulsed scheme, after an approximate π pulse on the quadrupole transition the quench beam at 854 nm is briefly switched on. We find that a quench pulse of just 2 μ s is sufficient for complete quenching of the $D_{5/2}$ state.

A 729 nm π -pulse length of about 10 μ s determines the amount of off-resonant excitation and thus the fidelity of the scheme: the target transition $|\downarrow\rangle$ to $D_{5/2}, m_J = +3/2$ is separated from the parasitic transition $|\uparrow\rangle$ to $D_{5/2}, m_J = +5/2$ by ~ 8 MHz for a magnetic field of 6.7 G. The frequency component of the Fourier transform of the effective square pulses (without any pulse shaping) already results in an expected pumping fidelity better than 99.6%, in agreement with the value for the combined pumping and readout fidelity (see below) in the experiment of 99.6%; figure 2(a). The cw scheme suffers from the fact that the presence of the quench beam hinders the coherent buildup of population in the $D_{5/2}$ state⁵.

4.2. Spin readout

A simple readout of the spin state by fluorescence observation is impossible because the Zeeman splitting of the spin levels $|\uparrow\rangle$ and $|\downarrow\rangle$ is smaller than the natural linewidth $\Gamma/2\pi \approx 22$ MHz of the corresponding 397 nm dipole transition. A scheme circumventing this by means of electromagnetically induced transparency has been proposed and experimentally realized [22], reaching a fidelity of 86%.

Our scheme reaches 99.6% fidelity and additionally shows a high robustness against imperfect laser settings or noise in the control parameters, still with a remarkably modest experimental effort. In a first step we apply a rapid adiabatic passage pulse (RAP) [12] where the amplitude is adiabatically switched on and off, and the frequency is chirped across

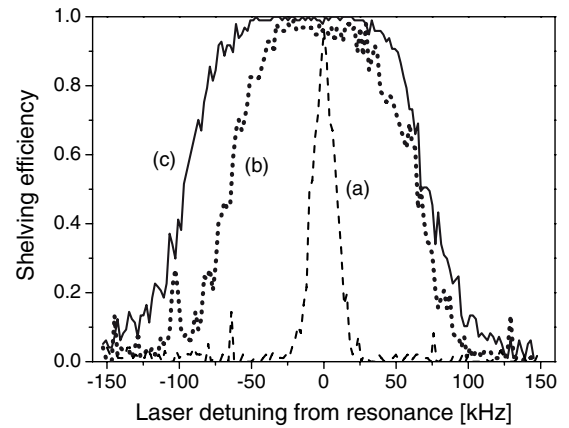


Figure 3. Transfer efficiency of the spin qubit $|\uparrow\rangle$ for various schemes versus central detuning of the readout pulse. (a) Dashed: the narrow peak is the result for a Gaussian pulse with a resonant pulse area of π . (b) Dotted: the much broader peak corresponding to a single RAP pulse shows that the robustness against frequency errors has greatly improved. (c) Solid: the curve for the double RAP shows that both performance and robustness have increased with respect to the single RAP.

resonance⁶. Even for an ion after Doppler cooling, a single RAP pulse on the $|\uparrow\rangle$ to $D_{5/2}, m_J = +5/2$ transition yields a fidelity of 95%; the leftover population in the $|\uparrow\rangle$ state is then transferred by a second RAP to the $D_{5/2}, m_J = +3/2$ state, and we reach a 99.6% readout fidelity with a high resilience against a drift of 729 nm laser frequency; see figure 3.

5. Raman transitions between the spin qubit levels

5.1. Raman spectroscopy and characterization of the transition

In our experiment, we use Raman beams derived from one laser source (see section 2). The laser is detuned from the

⁵ The quench laser couples the metastable state to the rapidly decaying $P_{3/2}$ state. Upon decay from this state, a photon is emitted which can be, in principle, detected, indicating that the system has ended up in the ground state. This represents an effective continuous measurement, disturbing the coherent evolution of the $S_{1/2}$ – $D_{5/2}$ superposition.

⁶ As stability against Rabi frequency errors is the main issue for readout robustification, we have also employed the SCROFOLOUS technique [23, 24] which is robustified by using a series of three π pulses with different phases. Although the technique was found to yield the same performance and an enhanced robustness against pulse area errors, the low resilience against the laser frequency drift strongly limited the practical use.

$S_{1/2} \rightarrow P_{1/2}$ resonance frequency by Δ , referred to as the Raman detuning. It is up to several tens of GHz and can be chosen to be both positive (blue detuning) or negative (red detuning). As Δ is very large compared to the Zeeman splittings within the $S_{1/2}$ and $P_{1/2}$ manifolds, which is on the order of 10–20 MHz, it can be considered constant for the different transitions between the Zeeman levels. The $P_{1/2}$ state can be adiabatically eliminated from the dynamics, giving an effective two-level system. The Raman Rabi frequency now reads $\frac{\Omega_1 \Omega_2}{2\Delta}$, where Ω_i are the resonant single-dipole Rabi frequencies associated with the individual beams.

A great advantage of the utilization of Raman transitions for quantum logic is the better control over the Lamb–Dicke factor. The difference k -vector of the beams strongly depends on the chosen geometry; see figure 1(a). In our setup, two different beam geometries are employed. In the first of these, a pair of Raman beams, R1 and CC, propagates parallel to each other and orthogonal to the magnetic field. The difference k -vector of the two beams is effectively zero, so the Lamb–Dicke factor is extremely small and electronic excitation is insensitive to the ion's motion. One of the beams (referred to as 'R1') is π -polarized, driving the $\Delta m_J = 0$ transition. The other beam (referred to as 'CC', cocarrier) is polarized orthogonal to the magnetic field. Therefore it yields two circular components, one of which contributes to the coherent dynamics of the effective two-level system if the Raman resonance condition is fulfilled, i.e. if the relative detuning of the beams matches the Zeeman splitting between the qubit levels. The alternative geometry consists of R1 and a beam propagating along the magnetic field direction (referred to as 'R2') such that the k -vector of the beat pattern is aligned along the trap axis. With no component of the k -vector in the radial plane of the trap, this Raman light field interacts only with the axial vibrational mode, and avoids any phonon-induced dephasing from the radial modes commonly called spectator modes. This fact is of tremendous importance for our microtrap with prospects to many ions, as we can drop the requirement of ground state cooling of all vibrational modes which would be experimentally undesirable.

From the beam geometry and the axial vibrational frequency, we deduce a Lamb–Dicke factor of $\eta = 0.21$, which is much larger than for the optical transition.

A Raman spectrum is shown in figure 4, clearly displaying the axial sidebands of motion for a single ion after Doppler cooling with $\bar{n} \sim 15$ quanta and an axial trap frequency of 1.35 MHz.

5.2. Raman Rabi oscillations on the carrier transition

Rabi oscillations driven by the R1/CC beams pair are shown in figure 5. Here, with $\eta = 0$, no phonon-induced dephasing can occur. For the experiment, we follow the sequence in section 2 without ground state cooling in step (b) and apply in step (c) both beams R1 and CC simultaneously for an interaction time t . The experiment is repeated 100 times, and the average excitation probability is plotted.

Showing no influence of the phonon number distribution, this technique provides an excellent opportunity for studying

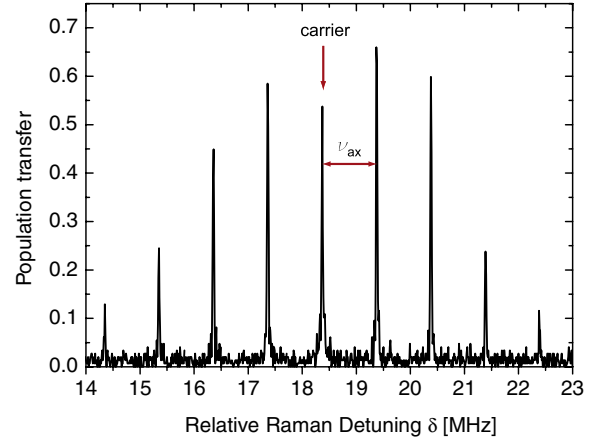


Figure 4. Raman spectrum obtained as R1 is fixed in frequency, and R2 is scanned over the sideband resonances. The excitation geometry leads to a difference k -vector along the trap axis, such that only axial, but no radial modes show up.

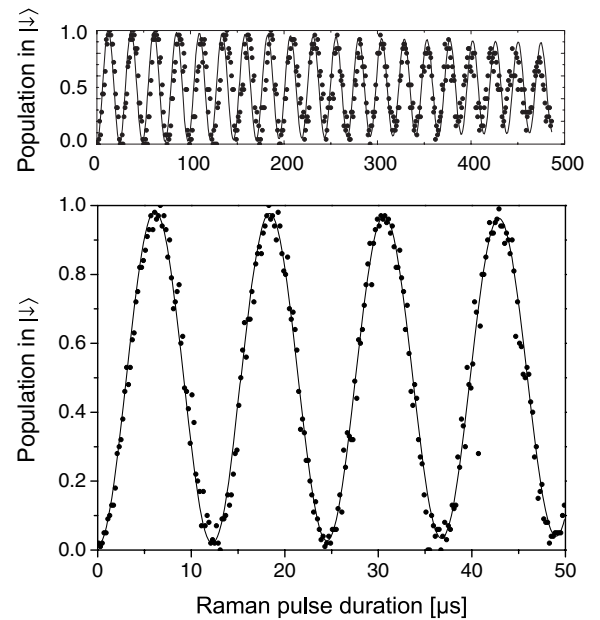


Figure 5. Rabi oscillations on the Raman transition driven by the R1/CC pair. No phonon-induced dephasing occurs because the Lamb–Dicke factor is virtually zero, which allows for driving many single-qubit rotations with high fidelity. The upper curve shows the long coherence time, while the lower curve displays the first four Rabi oscillations with high resolution. The two scans were taken with different Rabi frequencies.

other sources of decoherence. These are ambient magnetic field fluctuations, fluctuations of the relative phases of the beams due to air currents or mechanical vibrations and laser intensity fluctuations and spontaneous photon scattering. The latter two mechanisms scale with the total effective pulse area imparted to the ion on each of the dipole transitions pertaining to the Raman transition. Because of this, a Ramsey contrast measurement on a spin superposition created by R1/CC with fixed pulse areas and variable delay between the Ramsey pulses allows us to study the limits imposed by magnetic field noise and interferometric stability. Such a measurement has given a contrast of 90% after a delay time of 1.5 ms.

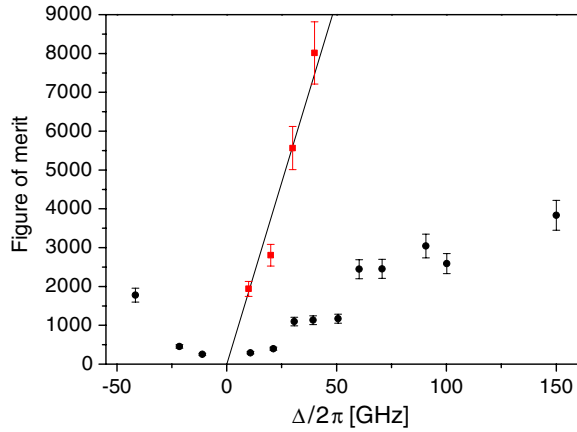


Figure 6. Rabi frequency divided by geometric mean of the scattering rates versus Raman detuning for the R1/CC pair (red squares) and the R1/R2 pair (black dots). The solid line through the R1/CC data is the theoretical value of $\sqrt{18}\Gamma^{-1}|\Delta|$.

As π -times of down to $2\ \mu\text{s}$ are routinely achieved, this separation of time scales appears sufficient for quantum logic experiments. We find in our setup that an air shield and the high passive mechanical interferometer stability of the optical setup are sufficient to avoid technically induced dephasing. The fundamental physical coherence limit of qubits is given by spontaneous photon scattering [25, 26].

During operations with the Raman beams, the small amount of population off-resonantly excited to the $P_{1/2}$ state decays with a rate corresponding to the inverse lifetime of this state, which results in random repopulation of the qubit levels. This off-resonant excitation reads for each beam i as $p_{P_{1/2}} = \Omega_i^2/2\Delta^2$, decreasing with the ratio of Rabi frequency and Raman detuning. Similar to far-detuned optical dipole traps [27], the photon scattering rate can be reduced if a large Δ is chosen at a high laser intensity. We investigated the photon scattering experimentally: for a given Raman detuning and fixed beam powers, the Rabi frequency is measured from Rabi oscillations as in figure 5 along with the scattering rates caused by each of the Raman beams individually. For this, the ion is initialized in $|\uparrow\rangle$, and one of the Raman beams is blocked. We apply the remaining Raman beam with a pulse of variable length. Finally, from the population in $|\downarrow\rangle$ we infer the scattering rate of beam i .

For the analysis, we normalize the measured Rabi frequency by the geometric mean of both scattering rates, such that in the resulting quantity, the individual Raman beam dipole coupling strengths Ω_i are cancelled.

A value of $\sqrt{18}\Gamma^{-1}|\Delta|$ is expected when the Clebsch–Gordan coefficients for the transitions are taken into account. The result is shown in figure 6, where the vertical axis can be interpreted as the number of Rabi cycles that could be driven on average before a single spontaneous scattering event occurs, in the absence of any other decoherence sources. The results for the R1/CC pair match very well the theoretical expectation. The fact that the values for the R1/CC pair match the theoretical expectation was initially not taken for granted because of the type of laser source used: a tapered amplifier generates a background of amplified spontaneous

emission whose width in the range of a few nm is given by the gain profile of the semiconductor laser medium. Through sum frequency generation, it is, in principle, possible that photons at frequencies $\omega_0 + n\omega_{\text{FSR}}$ are generated in the doubling stage, where ω_0 is the laser mode frequency, and ω_{FSR} is the free spectral range of the doubling stage. If such a frequency matches the direct optical $S_{1/2}$ to $P_{1/2}$ transition, resonant photon scattering would occur.

The same experiment, but with the R1/R2 pair of Raman beams, yields lower values for the Raman Rabi frequency. As in this geometry the excitation is sensitive to the motional degree of freedom along the trap axis, we attribute the lower value to the decrease of the Raman Rabi frequency with increasing phonon number and axial micromotion components⁷ at a trap drive frequency of 24.8 MHz.

Another characterization of the Raman interaction is done by the determination of the ac-Stark shifts, given by $\Delta_S = \Omega_i^2/4\Delta$ for one beam i . The absolute ac-Stark shift might be different for the two-qubit levels $|\uparrow\rangle$ and $|\downarrow\rangle$, leading to a differential shift. Under these circumstances, the quantum phase of qubit superpositions, or of multi-ion entangled states, evolves not only according to the desired gate operations, but shows an additional intensity-dependent rapid phase evolution. If this is the case, intensity fluctuations of the Raman lasers lead to qubit phase fluctuations, which represents an additional strong decoherence source.

The absolute ac-Stark shifts for all beams and qubit states is measured with the following procedure: first, the qubit is prepared either in the $|\uparrow\rangle$ or the $|\downarrow\rangle$ level by optical pumping with circularly polarized 397 nm laser light. Then, a superposition on the quadrupole transition is created by means of a $\pi/2$ pulse with the 729 nm laser, either with the $D_{5/2}, m_J = +5/2$ level for the $|\uparrow\rangle$ state or $D_{5/2}, m_J = +3/2$ level for the $|\downarrow\rangle$ state. A second $\pi/2$ pulse after a delay time of 50 μs concludes the Ramsey sequence. During this delay, a phase shift pulse from one of the Raman beams is irradiated on the ion, leading to a Ramsey fringe signal as the duration of the shift pulse is scanned. The absolute shift is then calculated from the fringe period t_R according to $\Delta_S = 2\pi/t_R$. For the R1 beam the $|\uparrow\rangle$ level is shifted by $2\pi \cdot 0.32(2)$ MHz, and the $|\downarrow\rangle$ level is shifted by $2\pi \cdot 0.33(2)$ MHz. Within the experimental errors, the differential shift from R1 vanishes. In contrast, we measured shifts from the R2 beam with $2\pi \cdot 0.17(2)$ MHz for the $|\uparrow\rangle$ level and $2\pi \cdot 0.29(2)$ MHz for the $|\downarrow\rangle$ level, resulting in a differential shift of about $2\pi \cdot 120$ kHz. Compensation of the differential shift is possible by proper adjustment of the polarization of the corresponding beam.

5.3. Resolved sideband cooling and blue sideband Rabi oscillations

Cooling close to the ground state of at least one vibrational mode is an essential prerequisite for two-ion gates, as even gate schemes for ‘hot’ ions require operation in the Lamb–Dicke

⁷ The presence of axial micromotion was confirmed by checking for RF echoes in the Raman spectrum of the R1/R2 pair, i.e. Raman resonances at relative detunings of $\omega_{\text{Zeeman}} + n\omega_{\text{RF}}$. Note that the effect of micromotion on the Raman Rabi frequency has even been used to allow the fine tuning of Rabi frequencies in quantum gate experiments with Be^+ ions [28].

regime, $\eta\sqrt{n} \ll 1$ [29]. For cooling close to the ground state one has to resort to a narrow transition with resolved motional sidebands [30], such that transitions to states with one less phonon (red sideband, RSB) can be driven preferentially and the $n = 0$ state acts as a dark state in which the population is finally trapped. In our system, we have two options to spectroscopically resolve sidebands, either the R1/R2 Raman transition or the quadrupole transition.

As the cooling always competes with the heating rate from trap-induced electric field noise, a high cooling rate is essential for a good cooling result. *A priori*, the Raman transition seems to be better suited for cooling because of the higher ratio of RSB to carrier Rabi frequency, which is essentially given by η on the decisive ‘bottleneck’ step from $n = 1$ to $n = 0$. This is because, ideally, the cooling rate is limited by off-resonant excitation of the carrier transition with subsequent spontaneous decay which can lead to the creation of one phonon. However, the problem arises in the dissipative step of cooling where the ion is repumped to the initial state to restart the RSB excitation. In the case of the Raman cooling scheme, the repumping is accomplished by the circular 397 nm beam which suffers from the spurious polarization error discussed in section 4.1. Therefore, the dark state $n = 0$ is not completely dark anymore, leading to a competing Doppler re-heating process which limits the attainable temperature.

In contrast, the sideband cooling on the $|\uparrow\rangle$ to $D_{5/2}, m_J = +5/2$ quadrupole transition does not suffer from this because the repumping is achieved by the quench laser near 854 nm, which does not interact with the ion anymore once one photon is spontaneously scattered. The cooling cycle is almost closed, because the decay from the $P_{3/2}$ state during the quench leads preferentially to the $|\uparrow\rangle$ level due to the selection rules. Only unlikely decay events into one of the D-states can lead to population of the $|\downarrow\rangle$ level. We utilize a pulsed sideband cooling scheme, since as for the qubit initialization, the power and frequency of the quench laser are no longer critical parameters then. The cooling pulse time is set such that an excitation maximum is reached on the RSB. This time typically ranges between $10\ \mu\text{s}$ and $20\ \mu\text{s}$, and increases as lower phonon numbers are reached because the RSB Rabi frequency scales as $\eta_{\text{ax}}\sqrt{n}$ with the phonon number n . After the RSB pulse, a quench pulse of typically $2\ \mu\text{s}$ completes the cooling cycle. After ten cooling cycles, about 10% of the population is accumulated in the wrong ground state spin level, such that a 397 nm repump pulse has to be employed. After eight such sequences, we employ a second cooling stage where the RSB pulse duration is increased, and the 729 nm optical pumping procedure is used instead of the circular 397 nm pulses. The longer time for repumping has no adverse effect on the cooling rate because it is used only every ten cycles.

5.4. Determination of the phonon number distribution

We confirm the sideband cooling result by employing either the quadrupole transition or the R1/R2 Raman transition. The optimization of the cooling is performed by minimizing the peak excitation of the RSB of the quadrupole transition, which is essentially given by the probability of not finding the ion

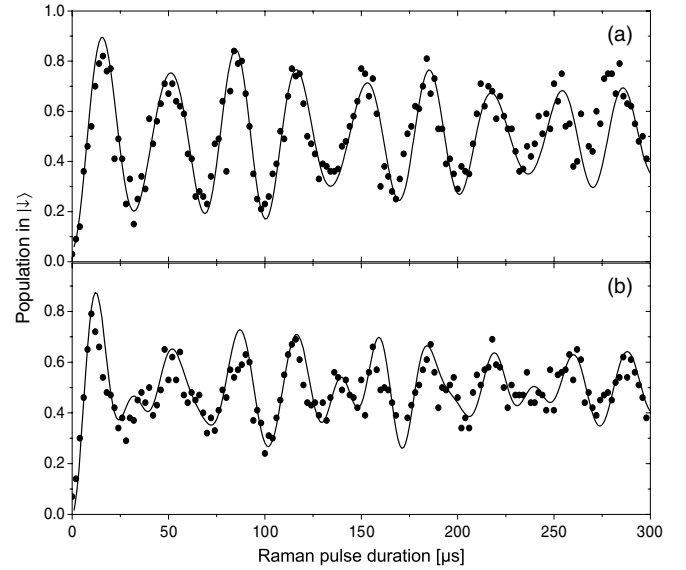


Figure 7. Coherent dynamics on the R1/R2 BSB after sideband cooling. The graphs show the population in the $|\downarrow\rangle$ level versus pulse duration of a square Raman excitation pulse (a) directly after sideband cooling, and (b) after a delay of 3 ms. The data were obtained with a Raman detuning of $\Delta \approx 40\ \text{GHz}$. The solid lines are reconstructed from the extracted phonon distribution data with the inclusion of a coherence decay time of $280\ \mu\text{s}$. We extract a mean phonon number of 0.24 for the data set without waiting time.

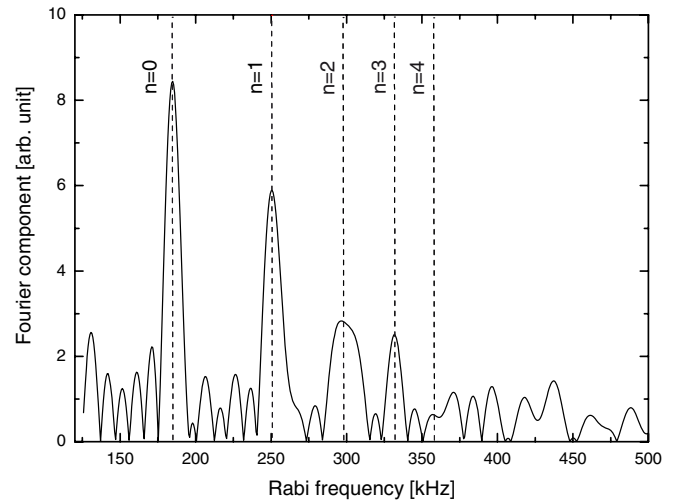


Figure 8. (a) Cosine transform of a R1/R2 pulse width scan on the BSB after a 3 ms delay between cooling and probing. The dashed lines indicate the different flopping frequencies given by the matrix element for the given transition.

in the ground state. For more accurate determination of the phonon number distribution we employ Rabi oscillations on the R1/R2 blue side band (BSB), with the advantage that no contributions from the radial vibrational modes can influence the result, and on the other hand the larger Lamb–Dicke factor of the Raman transition leads to a better separation of the Rabi frequencies for the various $n \rightarrow n + 1$ transitions. Excitation data are acquired until the oscillation contrast of the excitation signal has decreased beyond the projection noise limit for long pulse widths; see figure 7. The recorded traces

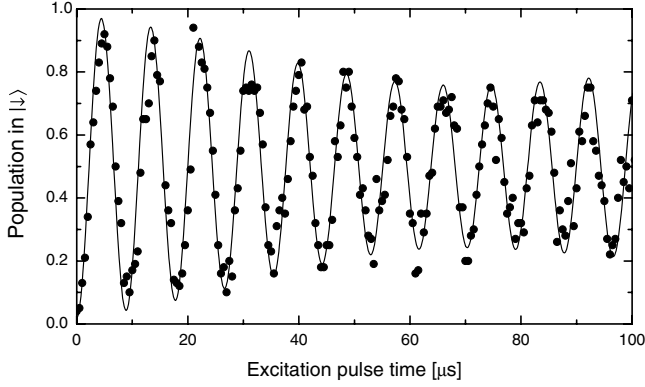


Figure 9. Coherent dynamics on the R1/R2 carrier transition after sideband cooling. The graph shows the population in the $|\downarrow\rangle$ state versus pulse duration of a square Raman excitation pulse directly after sideband cooling. The mean phonon number of 0.24 is used for fitting the data.

are analysed by a cosine transform to obtain the frequency components for the different contributing transitions, in full analogy to experiments on the cavity QED realization of the Jaynes–Cummings model [31]. Due to the finite data acquisition time, the peaks in the cosine transform pertaining to a given transition frequency are accompanied by aliases at other frequencies which lead to systematic errors when the phonon number occupation probability is inferred directly from the peak heights. A deconvolution procedure was used to remove this effect. The correctness of the method is proven by the fact that the method yields the correct input phonon number distribution when Monte Carlo generated data with realistic parameters are used. The resulting accuracy is then limited by the readout projection noise of the pulse width scan data.

A resulting spectrum is shown in figure 8. Upon proper normalization, the peak heights directly correspond to the occupation probabilities for the different phonon numbers. These data can then be used to reconstruct the coherent

dynamics, allowing for the empirical inclusion of a coherence decay time [32]. This is done according to

$$P_{|\downarrow\rangle}(t) = \sum_n \frac{P_n}{2} (A \cos(\Omega_{n,n+1}t) e^{-\gamma t} + 1), \quad (1)$$

where $P_{|\downarrow\rangle}(t)$ is the probability for finding the ion in $|\downarrow\rangle$, P_n is the phonon number distribution, $\Omega_{n,n+1}$ is the Rabi frequency pertaining to the specific BSB transition, A is the readout contrast and γ is the coherence decay rate. The coherence time $1/\gamma$ is found to be 280(20) μ s. The enhanced decoherence stems from spontaneous photon scattering [33]. The phonon distribution is reconstructed for various waiting times after sideband cooling in order to reveal the trap-induced heating dynamics. The time-dependent phonon number distribution is shown in figure 10, along with the resulting mean phonon number. This directly gives the lowest attainable mean phonon number of 0.24 and the heating rate to be 0.3(1) phonons ms^{-1} . This is about one order of magnitude better than earlier findings of 2.13 phonons ms^{-1} [10], which is attributed to an improved trap voltage supply.

The corresponding Rabi oscillations on the carrier of the R1/R2 Raman transition are shown in figure 9. Taking the phonon number after sideband cooling from the BSB Rabi oscillations, we find excellent agreement with the measurements made on the carrier transition.

6. Outlook

In the future, the full control of a single spin qubit demonstrated here will be extended to two-ion crystals. Then, a two-qubit quantum gate utilizing spin-dependent light forces will be used for the deterministic generation of Bell states. Taking advantage of the multi-segmented micro ion trap we intend to split the entangled two-ion crystal and investigate the separation of entangled states over distances of a few mm. As the lifetime of entangled Bell states in the decoherence-free basis states is long [19], measured to be a few seconds in

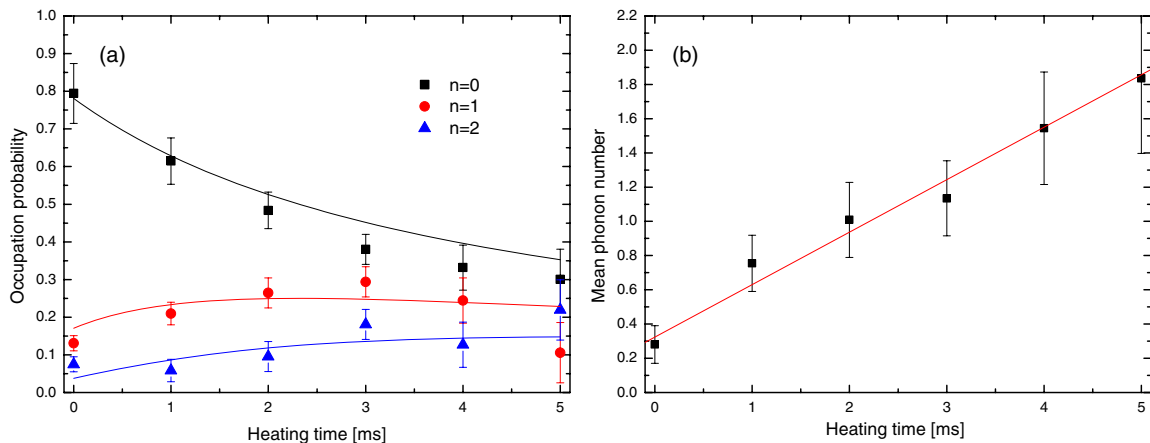


Figure 10. (a) Occupation probabilities P_n for the lowest vibrational levels $n \leq 2$, extracted from frequency spectra of the BSB pulse width scans (see figure 8) after different waiting times. For comparison, the solid lines show the occupation probabilities given by a thermal distribution $p(n) = \bar{n}^n / (\bar{n} + 1)^{n+1}$, where $\bar{n}(t)$ is given by a linear fit through the mean phonon numbers calculated from the data. (b) Mean occupation number \bar{n} calculated from P_n at different times after cooling. The linear fit indicates a constant heating rate of $\dot{n} = (0.3 \pm 0.1) \text{ ms}^{-1}$.

experiments using the Zeeman sublevels of $^{40}\text{Ca}^+$, we expect to be able to generate many of these Bell states within their coherence time. Protocols such as entanglement purification [34], entanglement swapping [35] and the generation of cluster states [36] will then be possible.

Acknowledgments

We acknowledge financial support by the German science foundation DFG within the SFB/TRR-21 and by the European commission within MICROTRAP (contract no 517675) and EMALI (contract no MRTN-CT-2006-035369).

References

- [1] Nielsen M and Chuang I L 2000 *Quantum Computation and Quantum Information* (Cambridge: Cambridge University Press)
- [2] European and the US quantum information roadmaps are found at <http://qist.ect.it> and at <http://qist.lanl.gov>
- [3] Roos C, Zeiger Th, Rohde H, Nägerl H C, Eschner J, Leibfried D, Schmidt-Kaler F and Blatt R 1999 Quantum state engineering on an optical transition and decoherence in a Paul trap *Phys. Rev. Lett.* **83** 4713
- [4] Roos C 2000 Controlling the quantum state of trapped ions *PhD thesis* Leopold-Franzens-Universität Innsbruck
- [5] Schmidt-Kaler F *et al* 2003 How to realize a universal quantum gate with trapped ions *Appl. Phys. B* **77** 789
- [6] Seidelin S *et al* 2006 A microfabricated surface-electrode ion trap for scalable quantum information processing *Phys. Rev. Lett.* **96** 253003
- [7] Häffner H *et al* 2005 Scalable multiparticle entanglement of trapped ions *Nature* **438** 643
- [8] Kielpinski D, Monroe C R and Wineland D J 2002 Architecture for a large-scale ion-trap quantum computer *Nature* **417** 709
- [9] Schulz S, Poschinger U, Singer K and Schmidt-Kaler F 2006 Optimization of segmented linear Paul traps and transport of stored particles *Fortschr. Phys.* **54** 648
- [10] Schulz S, Poschinger U, Ziesel F and Schmidt-Kaler F 2008 Sideband cooling and coherent dynamics in a microchip multi-segmented ion trap *New J. Phys.* **10** 045007
- [11] Gulde S, Rotter D, Barton P, Schmidt-Kaler F, Blatt R and Hogervorst W 2001 Simple and efficient photoionization loading of ions for precision ion-trapping experiments *Appl. Phys. B* **73** 861
- [12] Wunderlich C, Hannemann Th, Körber T K, Häffner H, Roos Ch, Hänsel W, Blatt R and Schmidt-Kaler F 2007 Robust state preparation of a single trapped ion by adiabatic passage *J. Mod. Opt.* **54** 1541
- [13] Monz T, Kim K, Hänsel W, Riebe M, Villar A S, Schindler P, Chwalla M, Hennrich M and Blatt R 2009 Realization of the quantum toffoli gate with trapped ions *Phys. Rev. Lett.* **102** 040501
- [14] Kirchmair G, Benhelm J, Zähringer F, Gerritsma R, Roos C F and Blatt R 2009 Deterministic entanglement of ions in thermal states of motion *New J. Phys.* **11** 023002
- [15] Benhelm J, Kirchmair G, Roos C F and Blatt R 2008 Experimental quantum information processing with $^{43}\text{Ca}^+$ ions *Phys. Rev. A* **77** 062306
- [16] Home J P, McDonnell M J, Lucas D M, Imreh G, Keitch B C, Szwer D J, Thomas N R, Webster S C, Stacey D N and Steane A M 2006 Deterministic entanglement and tomography of ionspin qubits *New J. Phys.* **8** 188
- [17] Home J 2006 Entanglement of two trapped-ion spin qubits *PhD thesis* Oxford University
- [18] Kielpinski D, Meyer V, Rowe M A, Sackett C A, Itano W M, Monroe C and Wineland D J 2001 A decoherence-free quantum memory using trapped ions *Science* **291** 1013
- [19] Häffner H *et al* 2005 Robust entanglement *Appl. Phys. B* **81** 151
- [20] Roos C F, Chwalla M, Kim K, Riebe M and Blatt R 2006 'Designer atoms' for quantum metrology *Nature* **443** 316
- [21] DiVincenzo D P 2000 The physical implementation of quantum computation *Fortschr. Phys.* **48** 711–83
- [22] McDonnell M J, Stacey J-P, Webster S C, Home J P, Ramos A, Lucas D M, Stacey D N and Steane A M 2004 High-efficiency detection of a single quantum of angular momentum by suppression of optical pumping *Phys. Rev. Lett.* **93** 153601
- [23] Cummins H K, Llewellyn G and Jones J A 2003 Tackling systematic errors in quantum logic gates with composite rotations *Phys. Rev. A* **67** 042308
- [24] Timoney N, Elman V, Glaser S, Weiss C, Johanning M, Neuhauser W and Wunderlich C 2008 Error-resistant single-qubit gates with trapped ions *Phys. Rev. A* **77** 052334
- [25] Ozeri R *et al* 2005 Hyperfine coherence in the presence of spontaneous photon scattering *Phys. Rev. Lett.* **95** 030403
- [26] Ozeri R *et al* 2007 Errors in trapped-ion quantum gates due to spontaneous photon scattering *Phys. Rev. A* **75** 042329
- [27] Grimm R, Weidemüller M and Ovchinnikov Y B 2000 Optical dipole traps for neutral atoms *Adv. At. Mol. Opt. Phys.* **42** 95
- [28] Turchette Q A, Wood C S, King B E, Myatt C J, Leibfried D, Itano W M, Monroe C and Wineland D J 1998 Deterministic entanglement of two trapped ions *Phys. Rev. Lett.* **81** 3631
- [29] Leibfried D *et al* 2002 Experimental demonstration of a robust, high-fidelity geometric two ion-qubit phase gate *Nature* **422** 412
- [30] Marzoli I, Cirac J I, Blatt R and Zoller P 1994 Laser cooling of trapped three-level ions: designing two-level systems for sideband cooling *Phys. Rev. A* **49** 2771
- [31] Brune M, Schmidt-Kaler F, Maali A, Dreyer J, Hagley E, Raimond J M and Haroche S 1996 Quantum Rabi oscillation: a direct test of field quantization in a cavity *Phys. Rev. Lett.* **76** 1800
- [32] Meekhof D M, King B E, Monroe C, Itano W M and Wineland D J 1996 Generation of nonclassical motional states of a trapped atom *Phys. Rev. Lett.* **77** 2346
- [33] Di Fidio C and Vogel W 2000 Damped Rabi oscillations of a cold trapped ion *Phys. Rev. A* **62** 031802
- [34] Pan J-W, Gasparoni S, Ursin R, Weihs G and Zeilinger A 2003 Experimental entanglement purification of arbitrary unknown states *Nature* **423** 417
- [35] Riebe M, Monz T, Kim K, Villar A S, Schindler P, Chwalla M, Hennrich M and Blatt R 2008 Deterministic entanglement swapping with an ion-trap quantum computer *Nat. Phys.* **4** 839
- [36] Briegel H J and Raussendorf R 2001 Persistent entanglement in arrays of interacting particles *Phys. Rev. Lett.* **86** 910